Fuel 411 (2026) 138083

Contents lists available at ScienceDirect

Fuel

journal homepage: www.elsevier.com/locate/fuel

Full Length Article

Numerical investigation of the thermal and mechanical response of PEMFCs under coupled loading conditions

Safiye Nur Ozdemir [a,*], Emre Kurt [b], Oguzhan Pektezel [c], Seçil Ekşi [a]

[a] Department of Mechanical Engineering, University of Sakarya 54050 Sakarya, Turkey
[b] Test and Analysis Department, Tırsan Solutions, Sakarya, Turkey
[c] Department of Mechanical Engineering, University of Balikesir 10145 Balikesir, Turkey

ARTICLE INFO

Keywords:
PEMFC
Numerical simulation
Thermo-mechanical analysis
Deformation
Flow-field design

ABSTRACT

Thermo-mechanical behavior of proton exchange membrane fuel cells (PEMFCs) subjected to combined clamping torque and thermal loading represents a critical factor governing their electrochemical performance, mechanical durability, and overall operational reliability. A comprehensive three-dimensional finite element model was developed for PEMFCs with four different flow field designs (spiral, serpentine, pin-type, and parallel) to investigate the coupled thermal and mechanical behavior of the cell components. A constant clamping torque of 10 Nm, which represents a typical value applied in practical single-cell assemblies, was imposed, and simulations were performed across operating temperatures of 50–80 °C. The results revealed that the pin-type flow field generated the highest stress levels, while the serpentine configuration exhibited the lowest, leading to approximately 5–6 % lower mechanical stresses and up to 39.2 % lower thermal stresses compared to the pin-type design. Directional deformation and stress analyses revealed that the serpentine flow field offers superior mechanical stability compared to the pin-type design, under both clamping and thermal loading conditions. Additionally, the maximum coupled thermo-mechanical stress remained well below the tensile strength limit of the membrane, indicating that the applied assembly conditions ensured safe operation without risk of structural damage. These findings underscore the importance of optimizing flow field geometry to achieve better stress uniformity, enhanced mechanical integrity, and longer service lifetime in PEMFCs. This study presents a novel comparative framework by simultaneously evaluating the thermo-mechanical response of multiple PEMFC flow-field geometries using a coupled finite-element approach, providing critical insights that can guide the optimization of thermo-mechanically robust channel designs.

1. Introduction

Proton exchange membrane fuel cells (PEMFCs) have gained considerable attention due to their high efficiency, low pollution emissions, and relatively low operating temperatures, making them suitable for transportation, portable, and stationary power applications [1–3]. In practical PEMFC assembly, the clamping torque applied to the bolts primarily determines the interfacial contact pressure and resistance at the MEA–GDL–bipolar plate interfaces, thereby influencing reactant distribution and sealing effectiveness. Meanwhile, thermal deformation occurs due to temperature gradients during operation, resulting from mismatches in thermal conductivity and thermal expansion coefficients among different cell components. These two simultaneously acting thermo-mechanical mechanisms critically affect stress uniformity, structural durability, and long-term operational reliability, ultimately shaping the energy efficiency and overall performance of PEMFCs. The electrochemical performance, efficiency, service life, and durability of PEMFCs are negatively affected during long-term operation due to thermal, mechanical, and chemical degradation mechanisms. PEMFCs fastened by a screw-assembly mechanism, stresses arising from clamping torque and operational thermal loads can induce structural defects such as cracks, as well as the formation of contact resistance and non-uniform distributions of reactants and water [4]. Ultimately, these factors can result in reduced efficiency, decreased durability, and a shorter service life. Therefore, investigating the reaction of PEMFC components to clamping torque and thermal loading is essential for determining optimal conditions to enhance cell performance, lifespan, and strength. Clamping torque is essential for achieving high cell performance and

* Corresponding author at: Department of Mechanical Engineering, University of Sakarya, TR-54050 Sakarya, Turkey.
E-mail address: safiyeozdemir@sakarya.edu.tr (S.N. Ozdemir).

https://doi.org/10.1016/j.fuel.2025.138083
Received 22 October 2025; Received in revised form 9 December 2025; Accepted 18 December 2025
Available online 22 December 2025

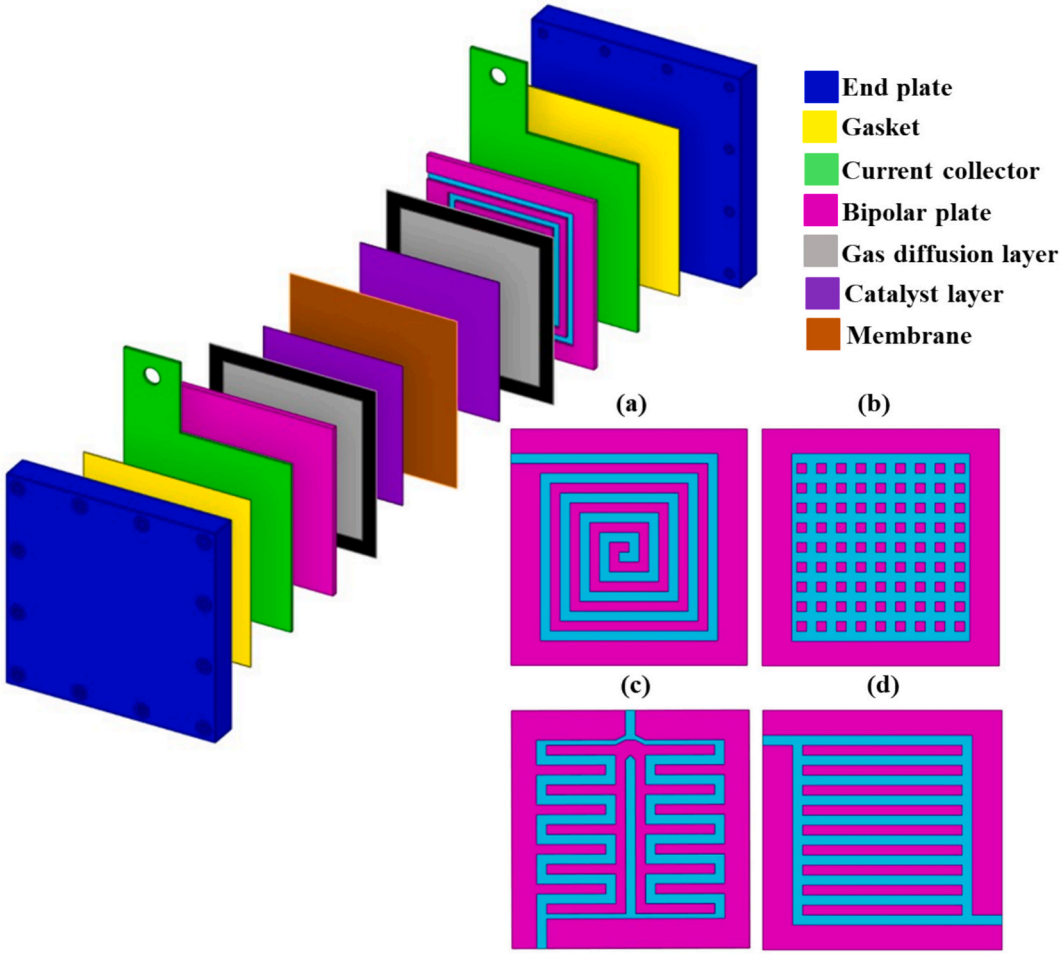

Fig. 1. Exploded view of the single-cell PEMFC assembly and different flow field configurations: (a) spiral, (b) pin-type, (c) serpentine, and (d) parallel.

Table 1
Physical and geometrical properties of the PEMFC components [33,34].

Property	End Plate	Sealing Gasket	Current Collector	Bipolar Plate	GDL	MEA
Dimensions (mm)	150 × 150	120 × 120	120 × 120	120 × 120	100 × 100	120 × 120
Thickness (mm)	20	0.26	2	4	0.26	0.155
Material	Steel	Silicon	Copper	Graphite	Carbon paper	Nafion
Elasticity modulus (MPa)	209,000	540	110,000	10,000	10,000	21
Poisson ratio	0.25	0.30	0.35	0.25	0.25	0.25
Thermal conductivity (W/mK)	44.5	0.517	385	95	17.122	0.455
Coefficient of thermal expansion (K^{-1})	$12 \bullet 10^{-6}$	$62 \bullet 10^{-6}$	$17 \bullet 10^{-6}$	$5 \bullet 10^{-6}$	$0.8 \bullet 10^{-6}$	$123 \bullet 10^{-6}$

ensuring the long-term reliability of the PEMFC [5]. In PEMFC technology, insufficient clamping torque leads to elevated contact resistance and mass transport resistance due to inadequate interfacial contact and non-uniform reactant distribution. Conversely, excessive torque can cause structural damage, particularly crushing delicate components such as the membrane and porous transport layers (PTLs), impairing gas diffusion and water management [6]. Therefore, optimum clamping torque is critical to ensure balanced mechanical integrity, minimized resistive losses, and maximum cell performance. Variable thermal loading may create localized hot spots due to temperature gradients in the membrane and electrodes, which can accelerate degradation and cause significant failure of cell components [7]. Mechanical stress distributions and deformations in PEMFCs, caused by temperature variations and applied clamping loads, can be explored through two primary approaches: experimental characterization and computational simulation. Mechanical stresses can be inferred through indirect techniques such as strain gauges, digital image correlation (DIC), fiber Bragg grating (FBG) sensors, and X-ray diffraction [8]. However, determining mechanical stress in PEMFC components experimentally is challenging due to the thin and fragile nature of the materials involved, along with the high costs and complexity associated with the necessary testing infrastructure. In contrast, full-scale Finite Element Method (FEM) simulations provide a cost-effective, efficient, and versatile way to conduct these analyses across a wide range of operating conditions [9–11]. When mathematical models are accurately constructed, FEM approaches yield high-resolution insights into thermo-mechanical stress distributions within the membrane and other cell components. Therefore, FEM simulations not only serve as a strong alternative to experimental techniques but are also essential tools for design optimization and durability assessment in PEMFC systems [12,13]. In existing literature, numerical and experimental studies have analyzed cell behavior under various operating conditions. Ouerghemmi et al. [14] conducted a

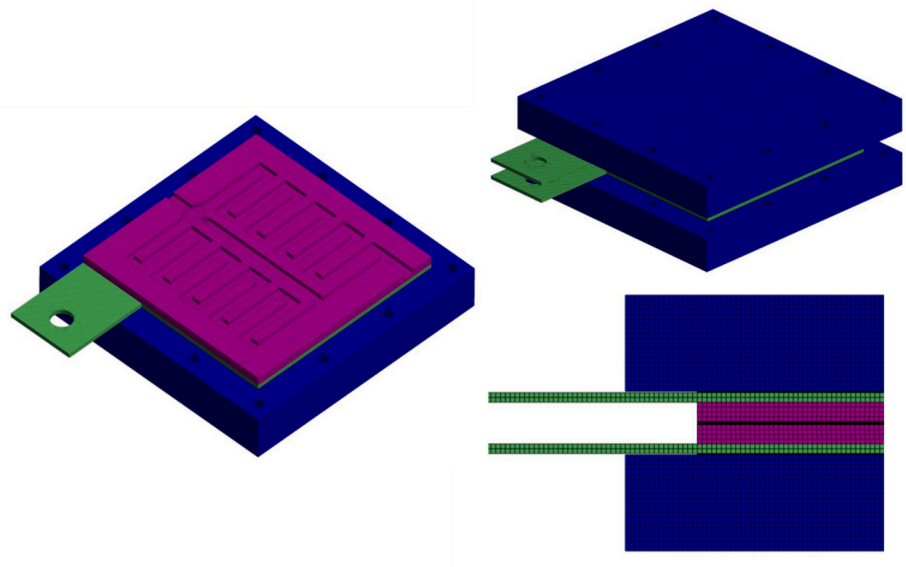

Fig. 2. Computational grid of the PEMFC model with a 3-D serpentine flow field.

Table 2
Grid convergence analysis.

Grid No.	Element Size (mm)	Maximum mechanical stress (MPa) on the membrane	Deviation (%)	Maximum thermal stress (MPa) on the membrane	Deviation (%)
G1	4	11.617	–	0.98574	–
G2	2.4	12.091	4.080	1.1092	12.525
G3	1.6	12.61	4.292	1.1689	5.382
G4	1	12.957	2.752	1.2061	3.182
G5	0.8	12.962	0.039	1.2063	0.017

numerical investigation into how temperature and relative humidity variations affect the mechanical response of the membrane electrode assembly (MEA), considering different assembly configurations of the PEMFC. Their findings revealed that bonded interfaces result in increased plastic deformation and stress accumulation within the membrane. In contrast, allowing interfacial sliding helps alleviate these issues. Additionally, they discovered that the type of porous transport layer (PTL) had only a minimal impact on the overall mechanical response. Notably, when paired with free interfaces, the fixed-force assembly mode significantly reduced membrane deformation and improved durability. Ma et al. [15] investigated the coupled effects of membrane mechanical degradation and contact resistance on PEMFC performance using both experimental measurements and numerical simulations. Their findings indicated that an optimal clamping pressure of 1 MPa provides the best balance among electrical conduction, thermal management, and reaction homogeneity, ultimately maximizing the cell performance. Varghese et al. [16] developed a full-scale three-dimensional simulation model for high-temperature proton exchange membrane fuel cells (HT-PEMFC) to analyze the thermomechanical stresses during the start-up process. Their study demonstrated that the high thermal expansion coefficient of the membrane induced compressive stresses exceeding 40 MPa. These stresses exceeded the mechanical strength limit of acid-doped polybenzimidazole (PBI) membranes, thereby identifying the membrane as the most vulnerable component of the system. Zhang et al. [17] employed a three-dimensional pore-scale model to examine the influence of assembly-induced compression on the PTL microstructure. Their results showed that as the compression ratio increased, the porosity of the PTL significantly decreased. Notably, at a 30 % compression ratio, the average pore size reduced by about 8.1 μm compared to the uncompressed state. Sun et al. [18] further investigated the impact of clamping force on PTL mechanical structure and the electrical (ECR) and thermal (TCR) contact resistances between the PTL and BP, based on numerical simulations validated against experiments. They found that ECR decreases as the compression torque increases. Additionally, at a compression pressure of 1.0 MPa, the power density was 1.1 % higher than at 1.5 MPa. Furthermore, TCR was shown to play a significant role in the thermal management of PEMFCs, although it had little effect on power density. Liu et al. [19] have introduced a novel pneumatic clamping mechanism designed to achieve uniform equivalent stresses, deformation distributions, and contact pressure distributions within the gas diffusion layer (GDL). Through comprehensive numerical simulations and experimental testing, this innovative design has significantly enhanced both the mechanical durability and electrochemical performance of PEMFCs. The findings reveal a substantial reduction in ohmic resistance, a 10 % increase in power density, and more uniform contact pressure distributions, indicating promising advancements in this area of research. Bates et al. [20] developed a full-scale 16-cell PEMFC stack and used FEM analysis to study the mechanical stresses caused by clamping pressure on the MEA and GDL. Their findings revealed a distinctly non-uniform stress distribution, with average stresses consistently lower in the cells adjacent to the end plates and progressively higher in those located near the center of the stack. Zhang et al. [21] proposed an equivalent stiffness model for a full-scale PEMFC stack composed of 10 cells. This model takes into account thermal expansions occurring under operational temperature conditions. The researchers validated the model experimentally by using pressure-sensitive films to measure the contact pressure distribution. The results showed that the deviation between the model predictions and the experimental data was within 5 %, with a maximum error of 4.41 %. Chippar et al. [22] conducted a coupled FEM–CFD study to evaluate the mechanical and electrochemical responses of HT-PEMFCs under different clamping conditions of the GDL. Their simulations revealed that higher compression forces led to pronounced GDL deformations, with irreversible plastic damage near the rib edges. Furthermore, the combined effects of GDL compression and intrusion significantly increased the spatial non-uniformity of reactant distributions and current density profiles, thereby highlighting the detrimental impact of excessive clamping on fuel cell performance. Wen et al. [23] demonstrated that among various bolt configurations and torque levels, the 6-bolt design at an assembly torque of 16 Nm achieved the most

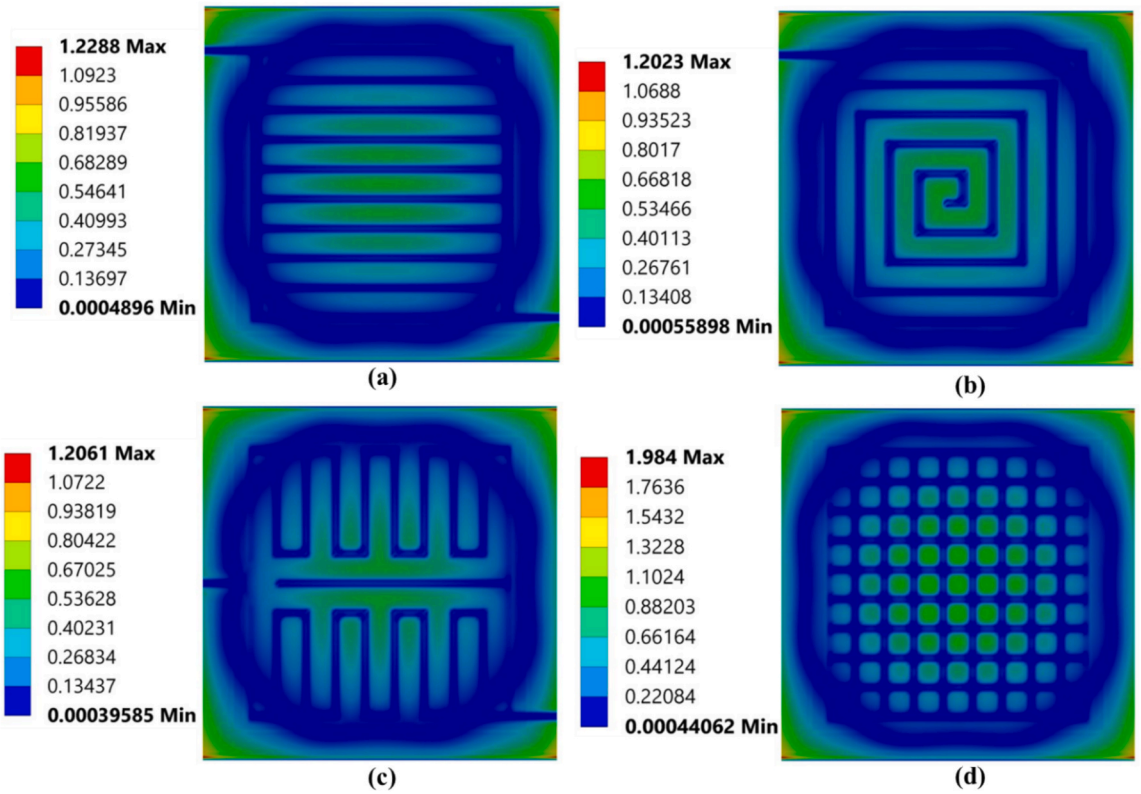

Fig. 3. Thermal stress distributions [MPa] on the membrane at a temperature of 50 °C for different flow field configurations: (a) parallel, (b) spiral, (c) serpentine, and (d) pin-type.

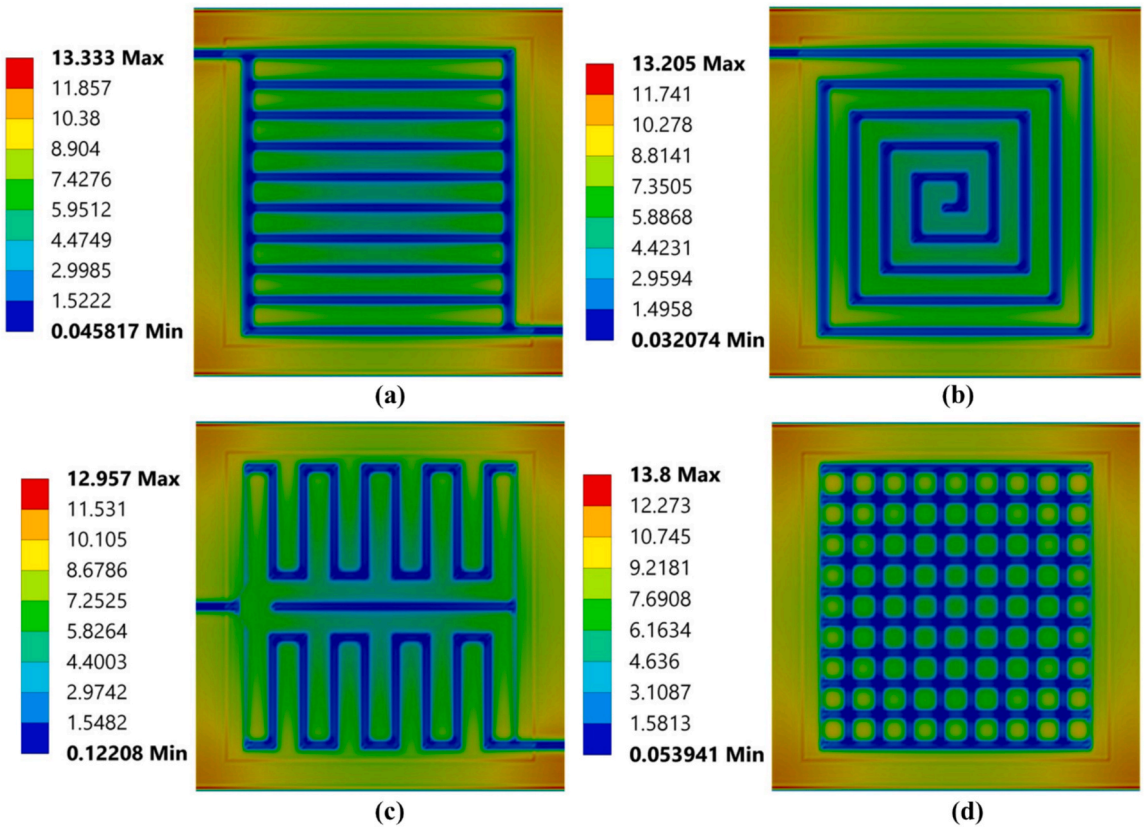

Fig. 4. Mechanical stress distributions [MPa] on the membrane under a clamping torque of 10 Nm for different flow field configurations: (a) parallel, (b) spiral, (c) serpentine, and (d) pin-type.

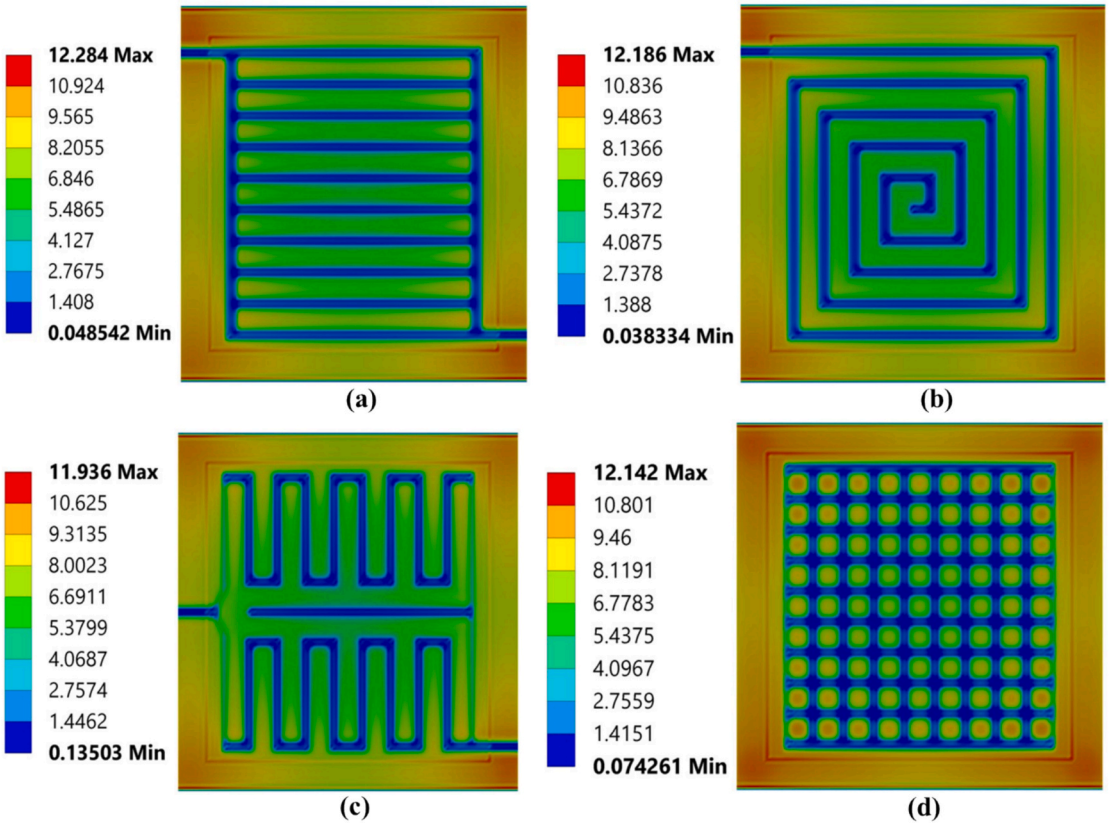

Fig. 5. Thermo-mechanical stress distributions [MPa] on the membrane under a clamping torque of 10 Nm and a temperature of 50 °C for different flow field configurations: (a) parallel, (b) spiral, (c) serpentine, and (d) pin-type.

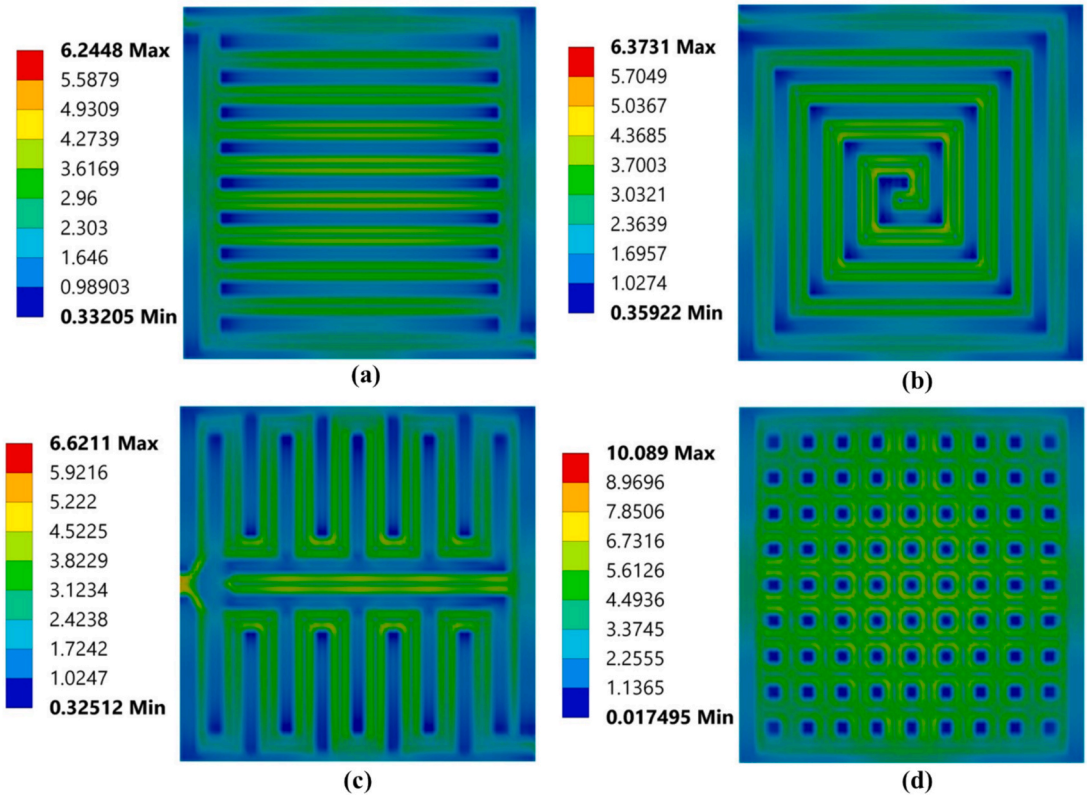

Fig. 6. Thermal stress distributions [MPa] on the cathode GDL at a temperature of 50 °C for different flow field configurations: (a) parallel, (b) spiral, (c) serpentine, and (d) pin-type.

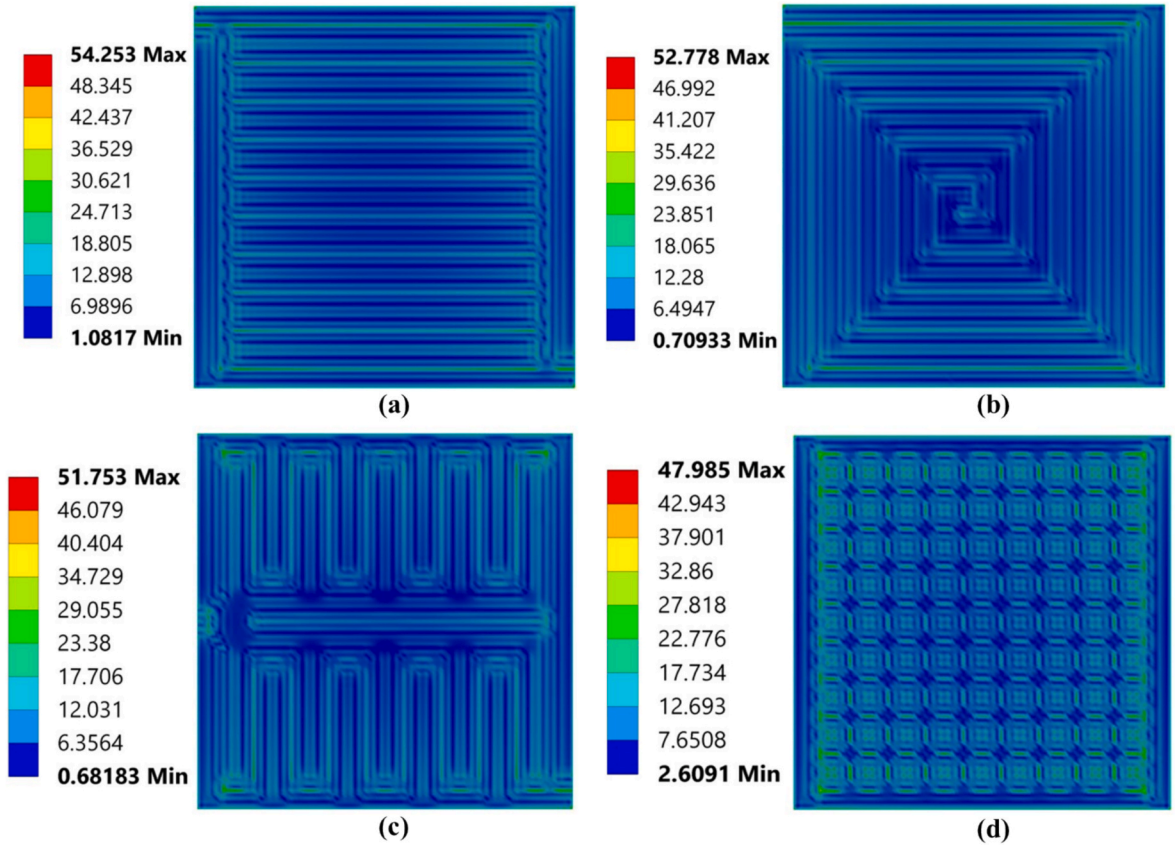

Fig. 7. Mechanical stress distributions [MPa] on the cathode GDL under a clamping torque of 10 Nm for different flow field configurations: (a) parallel, (b) spiral, (c) serpentine, and (d) pin-type.

uniform distribution of contact pressure and provided the highest performance in both single-cell and 10-cell PEMFC stacks. Movahedi et al. [24] developed a 3D FE model to study how assembly-induced deformations and displacements affect the polarization behavior of PEMFC with interdigitated flow fields. Their results reported that the optimum clamping pressure for a GDL thickness of 0.11 mm was around 0.5 MPa, at which the maximum current density of 1.293 A/cm^2 was achieved. Zhou et al. [25] introduced a numerical model to quantify the impact of mechanical degradation on the gas permeability of the membrane in PEMFC. Their findings indicated that mechanical damage accounted for approximately 7.3 % of the total permeation rate at a pressure of 130 kPa, while temperature effects were not considered. Jing et al. [26] numerically investigated the coupled effects of GDL deformation and ECR on PEMFC performance under different clamping pressures. Their results showed that the optimal clamping pressure depends strongly on the operating voltage range: within the low-voltage range, the best performance is achieved at 0.5–1 MPa; in the medium-voltage range, the optimum shifts to 2 MPa; whereas in the high-voltage range, the polarization curves nearly overlap, indicating that the influence of clamping pressure is negligible. Cha et al. [27] conducted experiments to evaluate the relationship between clamping force and water content in PEMFC. They found that high compression torque decreases the net drag coefficient. When this coefficient falls below 0.2, flooding can occur due to water accumulation on the cathode side. Wang et al. [28] conducted a study on the microscopic dynamic contact behavior within PEM fuel cell stacks under road-induced vibrations. They reported that the bipolar plate–membrane electrode assembly contact stiffness, governed by fractal dimension, characteristic length, and loading force, plays a key role in shaping the stack's natural frequencies. They also detected that higher clamping forces increase global modal frequencies while reducing local cell modal frequencies. Guan et al. [29] conducted a study on the influence of clamping load distribution on the pressure behavior of proton exchange membrane fuel cell stacks. They reported that uneven clamping load deteriorates durability and showed, through a combined experimental–FEM theoretical model with flexible pressure sensors, that their nacre-inspired optimization approach can significantly improve the nonuniform pressure distribution on bipolar plates. They also detected that the optimized design effectively enhances the internal contact pressure characteristics, providing a practical pathway for developing more durable and reliable fuel cell stacks. Pan et al. [30] conducted a study on the nonlinear contact pressure distribution between bipolar plates in proton exchange membrane fuel cells, emphasizing that bolt-induced nonuniformity can worsen under vibration and trigger localized corrosion and gas leakage. They proposed a woodpecker-inspired assembly design using a hyoid-shaped wave spring to achieve more uniform contact pressure, and verified its effectiveness through finite element simulations and experiments. They also detected that this design reduces pressure nonuniformity by up to 60 % and improves electrical performance, offering a reliable and low-cost solution for high-efficiency fuel cell stacks. Cai et al. [31] conducted a study on vibration-induced fretting corrosion of bipolar plates in proton exchange membrane fuel cells, highlighting that road-like vibration significantly accelerates surface degradation—an aspect overlooked in studies focused mainly on protective coatings. They reported that low-frequency vibration, reduced contact force, and high current density intensify heating, oxidation, and insulation on the bipolar plate surface, ultimately causing sharp performance loss. They also detected that vibration dramatically increases Joule heating at contact points, leading to electron transfer–induced melting and oxide accumulation. Guan et al. [32] conducted a study on the transient electrical contact failure of bipolar plates in proton exchange membrane fuel cells, developing a multiscale numerical model that incorporates surface oxide films to

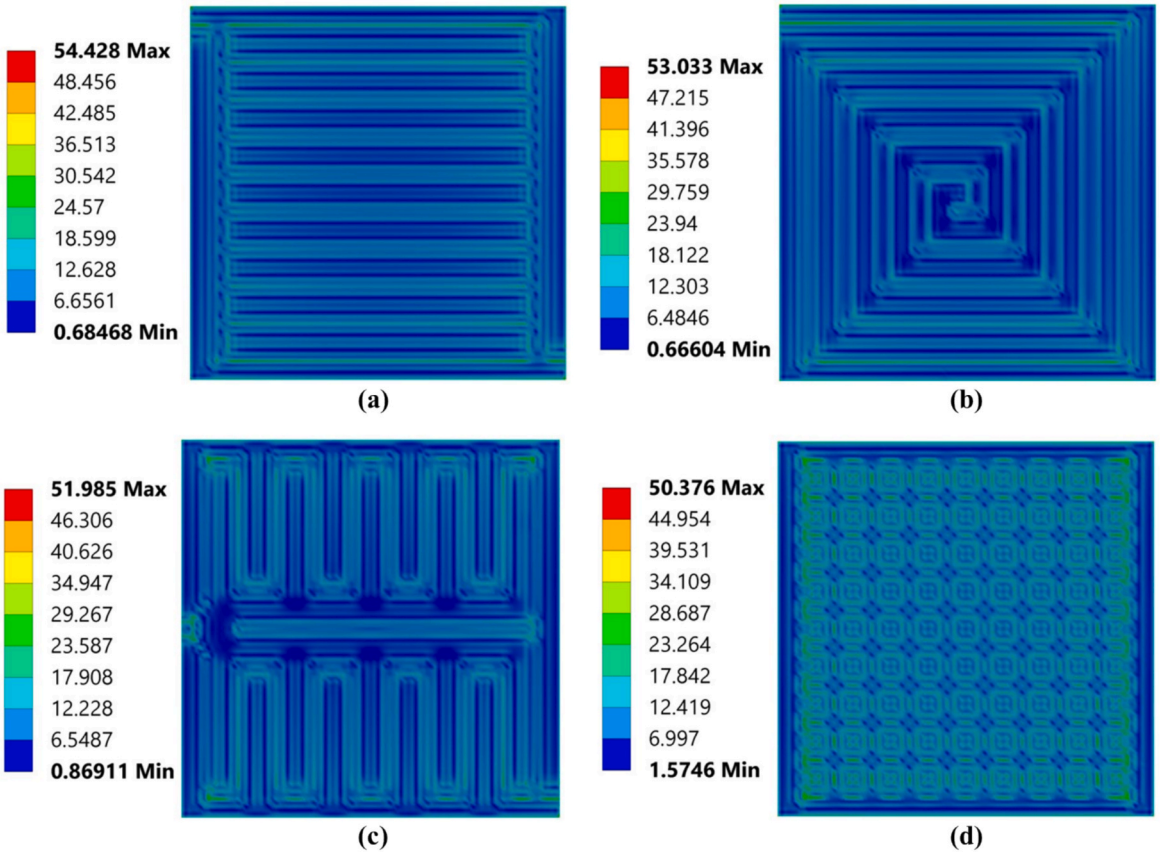

Fig. 8. Thermo-mechanical stress distributions [MPa] on the cathode GDL under a clamping torque of 10 Nm and a temperature of 50 °C for different flow field configurations: (a) parallel, (b) spiral, (c) serpentine, and (d) pin-type.

analyze the effects of vibration, current density, and normal load. They reported that low-frequency vibration significantly increases temperature rise, oxide-film models show nearly 27.9 % higher heating, and higher normal loads enhance contact stability by more than 67.4 %. They also detected that large contact currents generate extreme transient temperatures that accelerate oxide formation and electrical contact degradation.

Based on the above literature, much effort has been devoted to studying the effects of clamping torque and operating temperature on PEMFC performance, durability, and structural integrity. However, the detailed stress and deformation characteristics under the combined influence of clamping torque and dynamic thermal loading remain insufficiently understood, particularly regarding the role of flow-field geometry in determining thermo-mechanical responses. To bridge this gap, in the present study, comprehensive 3D finite element (FEM) models of single-cell PEMFCs featuring serpentine, parallel, spiral, and pin-type flow-field designs were developed. The proposed models enable a quantitative evaluation of the individual and coupled impacts of clamping torque and temperature on the thermal and mechanical behavior of key cell components, including the membrane, catalyst layers, and gas diffusion layers. This study differs from previous research, mainly concentrating on single loading conditions or specific geometries. It offers a systematic comparative analysis demonstrating how flow-field topology influences stress uniformity, deformation behavior, and overall structural stability. The findings of this research aim to enhance the design optimization and durability of PEMFCs by providing valuable insights into the thermo-mechanical coupling mechanisms operating under realistic assembly and operating conditions.

2. Model description

A three-dimensional model of PEMFC with an active area of 100 cm^2 is developed in ANSYS Workbench based on the finite element method (FEM). The schematic configuration of the single cell employed in this study and a 2-D schematic representation of different flow field configurations of PEMFC are shown in Fig. 1. As shown in Fig. 1, the flow channels are embedded in the bipolar plates on both the anode and cathode sides. The computational domain includes the catalyst-coated membrane, gas diffusion layers, flow channels, current collectors, sealing gaskets, and end plates. The physical and geometrical parameters of the numerical model are presented in Table 1.

2.1. Grid construction and independence assessment

In this study, the ANSYS Meshing built-in tool was utilized to mesh the full-scale three-dimensional numerical model of the PEMFC using hexahedral elements. Owing to the extremely thin geometry of the membrane and catalyst layers, a locally refined mesh was applied to these regions of the PEMFC model to improve the accuracy of thermo-mechanical stress predictions and ensure accurate resolution of temperature- and load-induced gradients. The computational grid and the detailed meshing structure of the PEMFC model with a serpentine flow field are illustrated in Fig. 2. Moreover, to ensure mesh independence and identify the optimal mesh density that provides a balance between computational cost and solution accuracy, thermal and mechanical stresses were employed as evaluation criteria to assess the stability of the simulation results by monitoring variations with increasing element counts. The grid independence analysis revealed that further refinement beyond 1,351,084 cells led to less than a 1 % variation in thermal and mechanical stresses, as presented in Table 2. Consequently, the G4 grid

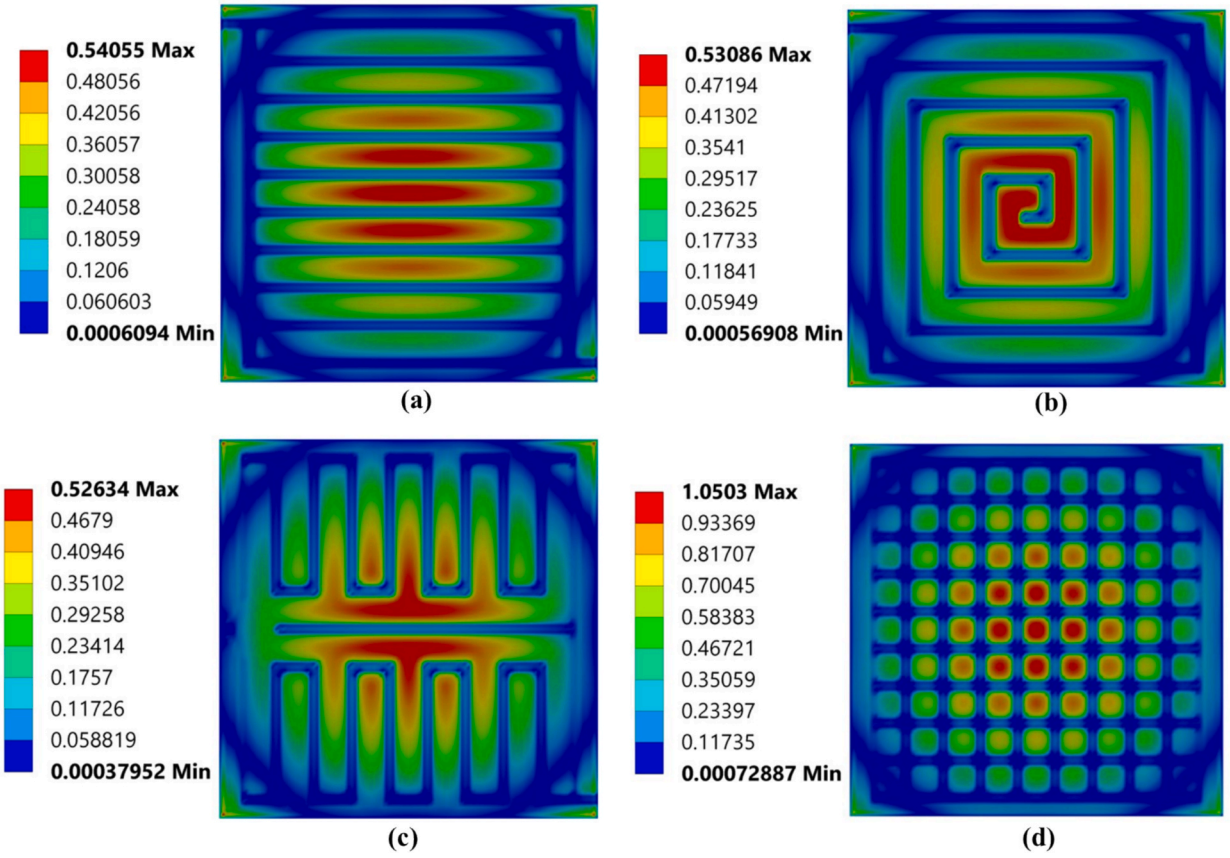

Fig. 9. Thermal stress distributions [MPa] on the cathode CL at a temperature of 50 °C for different flow field configurations: (a) parallel, (b) spiral, (c) serpentine, and (d) pin-type.

configuration, corresponding to a uniform element size of 1 mm, was adopted for all subsequent simulations to ensure an optimal balance between computational load and accuracy. Table 2 demonstrates that both thermal and mechanical stresses converged quickly with mesh refinement, and the differences between the final two grid levels remained below 0.05 %, confirming that the numerical model achieved grid independence.

2.2. Model assumptions, governing equations, and boundary conditions

The steady state heat conduction in the solid domains is described as [35],

$$\frac{\partial}{\partial x}\left(k^{eff}\frac{\partial T}{\partial x}\right)+\frac{\partial}{\partial y}\left(k^{eff}\frac{\partial T}{\partial y}\right)+\frac{\partial}{\partial z}\left(k^{eff}\frac{\partial T}{\partial z}\right)+S_T=0 \quad (1)$$

where k^{eff} is the effective thermal conductivity, T is the temperature, and S_T is the volumetric heat generation.

The thermal strain caused by thermal expansion resulting from temperature variation is expressed as [36],

$$\varepsilon^T=\alpha\Delta T \quad (2)$$

where α is the thermal expansion coefficient and ΔT is the temperature variation.

The total strain in each principal direction, accounting for both mechanical and thermal effects, is defined as:

$$\begin{cases}\varepsilon_x=\frac{1}{E}\left[\sigma_x-\mu(\sigma_y+\sigma_z)\right]+\alpha\Delta T\\ \varepsilon_y=\frac{1}{E}\left[\sigma_y-\mu(\sigma_x+\sigma_z)\right]+\alpha\Delta T\\ \varepsilon_z=\frac{1}{E}\left[\sigma_z-\mu(\sigma_x+\sigma_y)\right]+\alpha\Delta T\end{cases} \quad (3)$$

where μ is Poisson's ratio, E is the elasticity modulus, σ_x, σ_y, and σ_z are normal stress components.

The stress state of the components was evaluated using the von Mises criterion [37,38].

$$\sigma=\sqrt{\frac{1}{2}\left[(\sigma_x-\sigma_y)^2+(\sigma_y-\sigma_z)^2+(\sigma_z-\sigma_x)^2+6\left(\tau_{xy}^2+\tau_{yz}^2+\tau_{zx}^2\right)\right]} \quad (4)$$

An effective convection was applied to the outer surface of the numerical model, with a heat transfer coefficient specified as 65 W/m^2·K. Initially, the ambient temperature is set to 22 °C. In the thermo-mechanical model, the fluid domains within the anode and cathode flow channels were not explicitly resolved. Instead, isothermal boundary conditions were applied to the channel walls to represent the set operating temperature. In the end plate bolt holes, the x and y degrees of freedom are considered fixed, while the z degree of freedom is considered free. Each bolt hole on the anode end plate was subjected to a positive axial loading in the z-direction, whereas the bolt holes on the cathode end plate were loaded in the opposite axial direction. Mechanical loading was applied as a constant clamping torque of 10 Nm to the bolt holes of the end plates [39]. To prevent sliding or rotation between the layers of the PEMFC, no-slip conditions were applied at all contact interfaces. The axial force exerted on the bolts was calculated using the following equation.

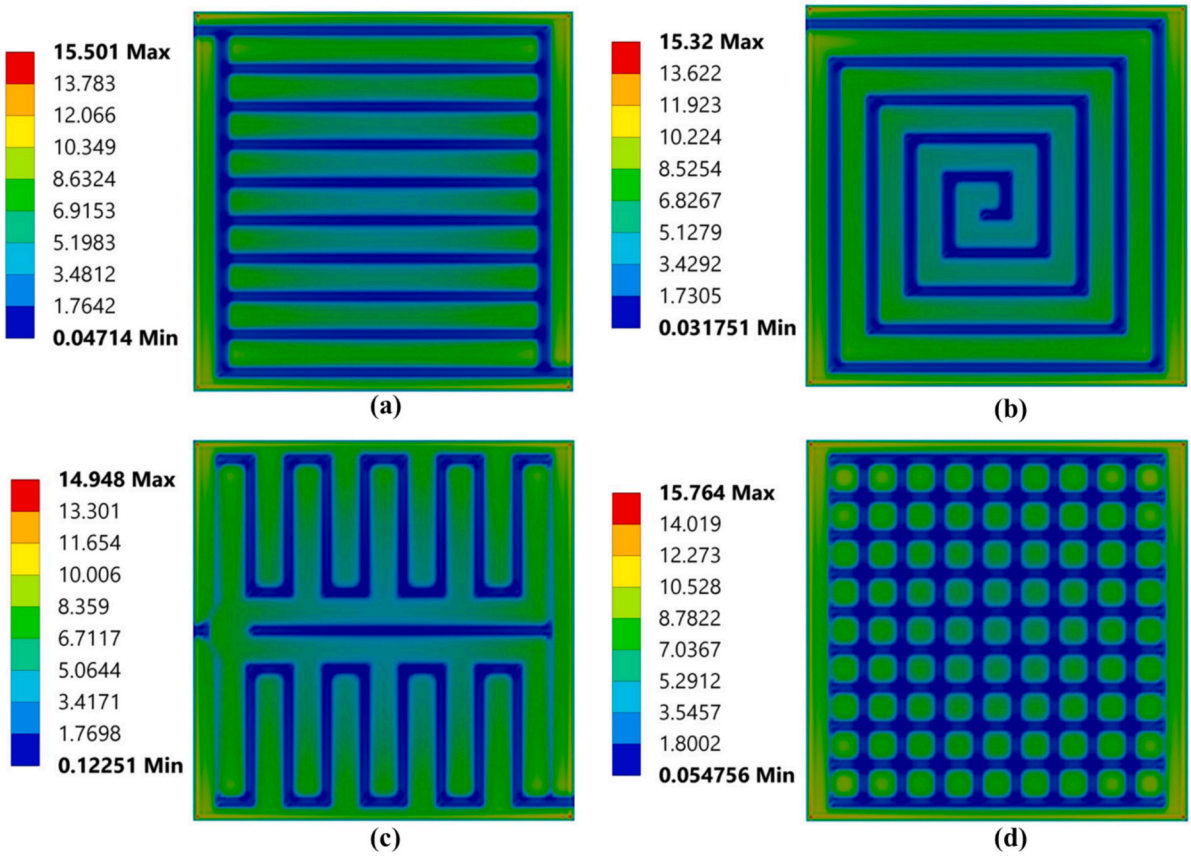

Fig. 10. Mechanical stress distributions [MPa] on the cathode CL under a clamping torque of 10 Nm for different flow field configurations: (a) parallel, (b) spiral, (c) serpentine, and (d) pin-type.

$$F = \frac{\tau \bullet N}{C \bullet D} \tag{5}$$

where D is the diameter of the bolt, N is the number of bolts, C is the friction coefficient (taken as 0.2 for steel bolts), and τ is the clamping torque. The axial force was uniformly applied over the bearing surfaces of the bolt holes on the end plates to represent the mechanical load transfer during assembly accurately.

To assess the influence of temperature on the thermal response of the cell components, simulations were performed at operating temperatures of 50, 60, 70, and 80 °C. The thermal source in the FEM model comes from the reactant gases: hydrogen on the anode side and air on the cathode side, which flow through the channel domains. To represent the thermal energy provided by the hot reactant streams during PEMFC operation, isothermal boundary conditions were applied to the inner walls of the channels.

3. Results and discussion

This section presents a comprehensive numerical analysis of the thermal, mechanical, and coupled thermo-mechanical behavior of deformable PEMFC components—membrane, catalyst, and GDL—under various flow-field geometries and loading conditions. The study systematically evaluates the influence of clamping torque and operating temperature on stress distribution, deformation, and structural integrity, while also examining temperature uniformity across the active area under realistic operating conditions. The findings offer valuable insights into the relationship between mechanical compression and thermal expansion, providing design guidelines to enhance the durability and performance of PEMFC assemblies. As illustrated in Fig. 3, the comparative analysis of thermal stress distributions shows that the flow field configuration influences the thermal durability of PEMFC membranes. At a temperature load of 50 °C, and without considering the effect of clamping torque in the numerical model, the maximum stresses on the membrane are calculated as 1.2288 MPa for the parallel, 1.2023 MPa for the spiral, 1.2061 MPa for the serpentine, and 1.984 MPa for the pin-type configuration. While Nafion-based membranes typically have an ultimate tensile strength of 20–30 MPa under hydrated conditions, these stress levels may not lead to immediate fracture. However, they signify critical sub-threshold loads that can accelerate fatigue-driven degradation [40]. A non-reinforced perfluorosulfonic acid membrane, Nafion 115, served as the proton-conducting electrolyte in this study. Hydrocarbon-based PEMs, such as polyphenylene-based Pemion®, exhibit distinct differences in thermo-mechanical properties when compared to Nafion. Nafion shows a low hydrated elastic modulus of approximately 20–30 MPa, as reported by Kundu et al. [41], and a relatively high coefficient of thermal expansion (CTE) ranging from 110 to 180 $\times 10^{-6}$ K^{-1}, depending on hydration [37]. In contrast, Pemion® technical datasheet [42] reports an in-plane Young's modulus of 650–800 MPa, which is an order of magnitude higher than that of hydrated Nafion. Hydrocarbon-based membranes such as Pemion® are built on an aromatic polyphenylene backbone. According to the Polymer Data Handbook [43], high-performance aromatic polyarylene polymers exhibit a coefficient of thermal expansion in the range of 22–38 $\times 10^{-6}$ K^{-1}, which is substantially lower than that of Nafion. Repeating the current simulations with hydrocarbon membrane properties would result in less thermal deformation, increased mechanical stress concentrations, and better dimensional stability. This would alter the thermo-mechanical response while maintaining the same qualitative trends observed. Although viscoplastic relaxation can become significant at temperatures above approximately 100 °C, the temperature range of 50–80 °C examined in this study ensures that the Nafion

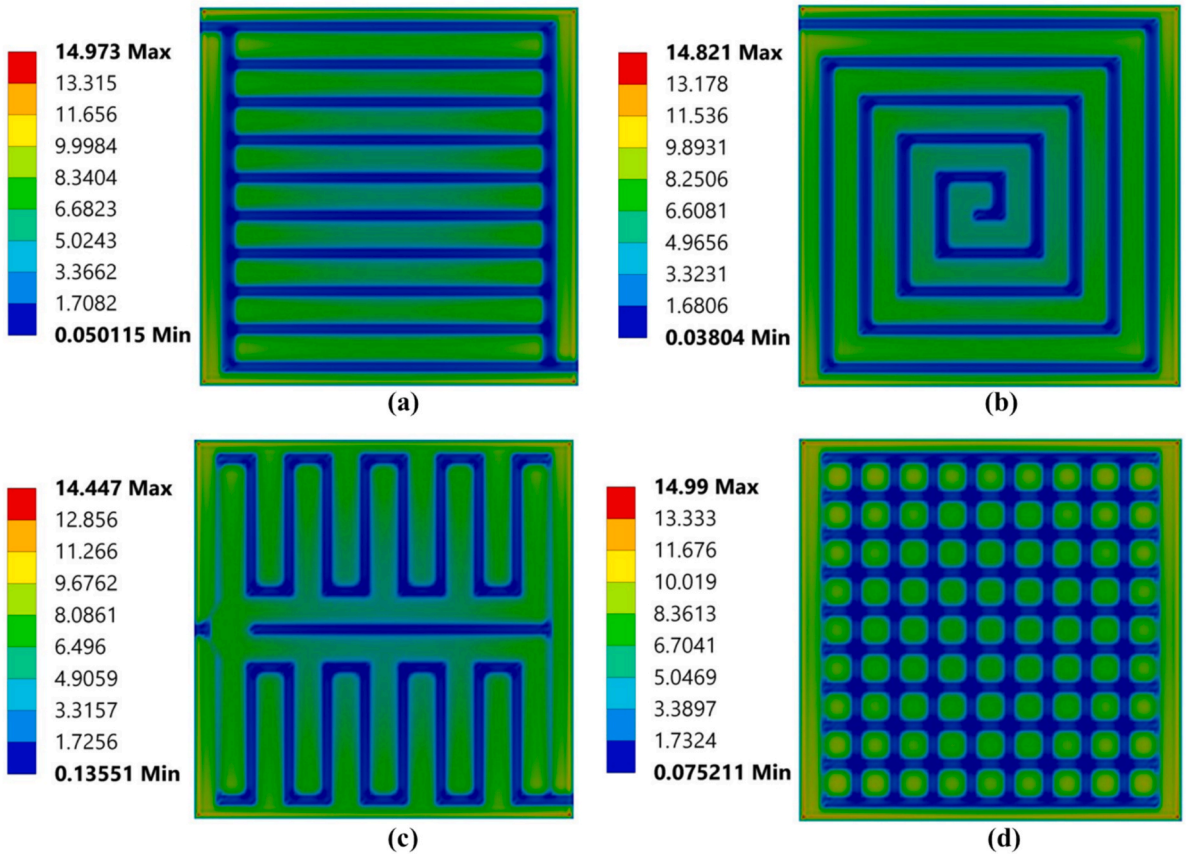

Fig. 11. Thermo-mechanical stress distributions [MPa] on the cathode CL under a clamping torque of 10 Nm and a temperature of 50 °C for different flow field configurations: (a) parallel, (b) spiral, (c) serpentine, and (d) pin-type.

membrane remains primarily elastic. Therefore, while a temperature-dependent viscoelastic model might slightly lower the maximum stresses, the current material assumptions are still appropriate for assessing the relative effects of flow-field geometry. Due to temperature fluctuations and the associated variations in the thermal expansion coefficients of PEMFC components, the highest thermal stresses were observed in the pin-type configuration, while the lowest values were recorded in the spiral design. In particular, the pin-type flow field creates approximately 65 % higher stresses compared to the spiral configuration. Sustained high levels of thermally induced stress in the membrane increase the risk of microcrack initiation, which can adversely affect the durability, mechanical integrity, electrochemical performance, and overall energy efficiency of the PEMFC [44]. Optimizing flow-field geometry enhances mass transport, water management, and thermal stability, ultimately extending the service life of PEMFC stacks.

The lower thermal stress circle, consistently observed in all configurations, is a natural thermo-mechanical phenomenon caused by the dominant path of heat conduction through the end plates. Since the end plates have significantly higher thermal conductivity than the membrane, gas diffusion layer, and catalyst layers, the heat generated in the active area is preferentially directed toward the bolt-supported structural backbone of the cell. This enhanced capacity for heat conduction limits local temperature increases and reduces thermal gradients near the center of the assembly. Because thermo-elastic stress is directly influenced by differential thermal expansion, this region, where heat is conducted more effectively, inherently exhibits lower stress levels across all geometries, regardless of the channel design.

To better evaluate the interaction between mechanical loading and the thermal response of the membrane, the following analysis emphasizes the distribution of mechanical stresses caused by the applied clamping torque. The structural analysis results in Fig. 4 show the distribution of mechanical stress on the membrane for different flow-field configurations with a clamping torque of 10 Nm. Due to the strong interfacial contact between the bipolar plate and the membrane–electrode assembly (MEA), stress concentration occurs particularly near the corners of the membrane, where the clamping torque is transmitted through the bolt regions. In contrast, the central areas of the membrane show relatively uniform and lower stress levels, indicating that the applied load is effectively distributed across the active surface. Among the investigated flow-field geometries, the pin-type configuration generated the highest mechanical stresses on the membrane, whereas the serpentine pattern resulted in the lowest. Accordingly, the mechanical stresses decreased by approximately 6.1 % when transitioning from the pin-type to the serpentine design, indicating a more homogeneous pressure distribution and improved mechanical stability in the latter case. From FEM results, this reduction indicates that the serpentine flow-field configuration provides a more uniform stress distribution, effectively alleviating localized compressive loads and thereby reducing the likelihood of mechanical fatigue or structural degradation during prolonged operation. Moreover, the maximum mechanical stress, measured at approximately 13.8 MPa, remains significantly below the tensile strength threshold of the Nafion membrane, confirming that the applied clamping conditions do not pose any risk of mechanical failure, plastic deformation, or interfacial delamination [41].

While mechanical loading provides insight into the stress distribution resulting from clamping, it does not account for the additional strain effects arising from variations in operational temperatures. To comprehensively evaluate the combined impact of torque and thermal expansion, we conducted coupled thermo-mechanical simulations. Fig. 5 illustrates the thermo-mechanical stress distributions on the

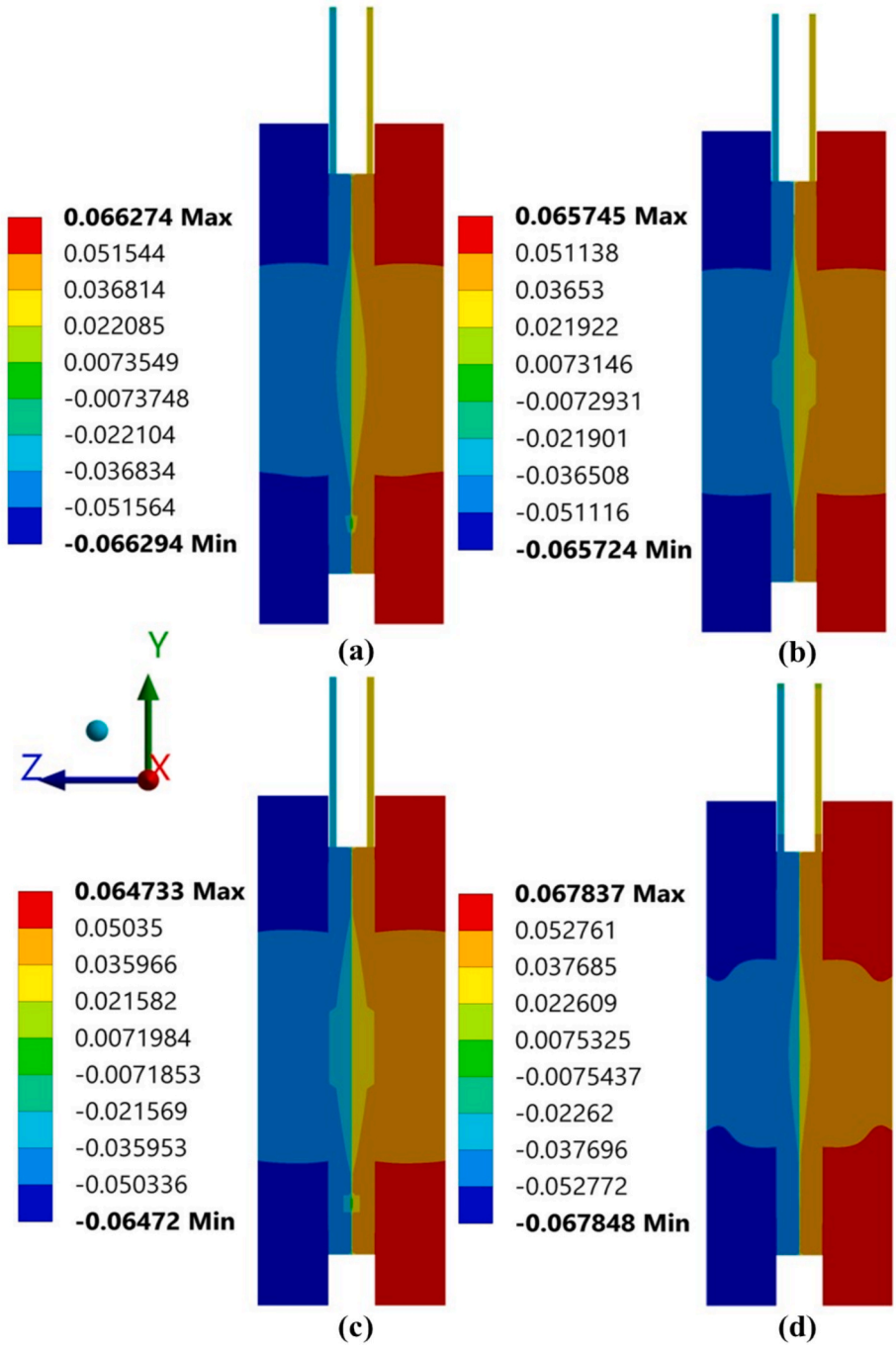

Fig. 12. Directional deformation distributions [mm] of the PEMFC under a clamping torque of 10 Nm for different flow field configurations: (a) parallel, (b) spiral, (c) serpentine, and (d) pin-type.

membrane due to the combined effect of a 10 Nm clamping torque and an operating temperature of 50 °C. The numerical analysis indicates that the thermo-mechanical stresses are lower than those generated by mechanical compression alone. This stress reduction is attributed to opposing deformation mechanisms: the clamping torque causes the membrane structure to contract inward. At the same time, applying a temperature load induces thermal expansion of the materials, resulting in outward deformation. These two effects partially cancel the overall stress magnitude, reducing stress intensity and leading to a more uniform stress distribution across the membrane surface. The differences in thermo-mechanical behavior among the four flow-field configurations can be attributed to the relationship between the percentage of flow-channel area and the stiffness of the mechanical support provided by the solid rib regions. A larger channel-area ratio decreases solid contact between the membrane and the flow-field plate, limiting lateral heat conduction and increasing localized hot spots. The resulting temperature gradients lead to non-uniform thermal expansion and higher thermal stresses. In contrast, as the rib-supported area increases, the membrane benefits from more effective heat spreading and greater structural support, which reduces deformation mismatch and stress levels. For example, the serpentine layout features more continuous supporting rib structures, which facilitate better heat dissipation and consequently lower thermo-mechanical stresses.

Beyond the membrane, the GDL plays an essential structural role in enabling load and heat transfer between the catalyst layer (CL) and the bipolar plate. To gain a deeper understanding of how coupled stresses

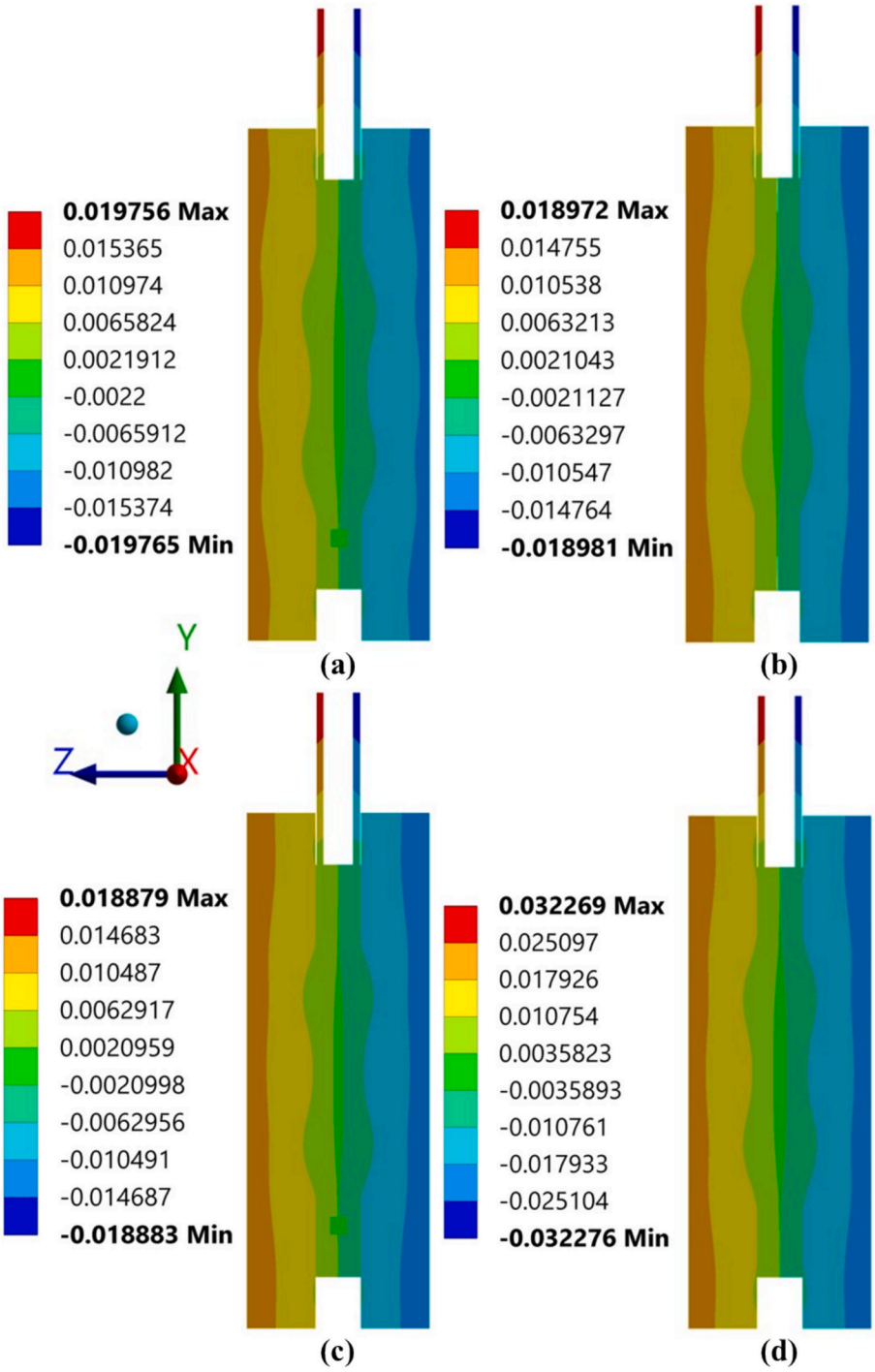

Fig. 13. Directional deformation distributions [mm] of the PEMFC at a temperature of 50 °C for different flow field configurations: (a) parallel, (b) spiral, (c) serpentine, and (d) pin-type.

are conducted through adjacent layers, we thoroughly examined the thermal and mechanical behavior of the GDL. The GDL is a vital structural and functional component in PEMFCs, facilitating the transport of reactant gases, product water, and electrons between the catalyst layer and bipolar plate [45]. In this study, a carbon paper–type GDL (Sigracet) was employed due to its favorable properties, including high electrical conductivity, good gas permeability, and adequate mechanical compliance. However, its porous structure makes it susceptible to deformation under the applied clamping force.

In Fig. 6, Sigracet carbon paper was chosen as the GDL material. Numerical analyses indicate that temperature variations induce thermal stresses on the GDL. Specifically, all four flow-field configurations yield stress magnitudes below the tensile strength limit of the carbon paper, indicating that no structural degradation or mechanical failure occurs in the GDL during operation [46].

After conducting thermal analysis, we examined how mechanical compression impacts the GDL domain to measure the additional stress from the applied torque. Fig. 7 illustrates the mechanical stress distributions on the cathode GDL for different flow-field configurations under a 10 Nm clamping torque. The results indicate that the maximum mechanical stress increases significantly with the intensity of compression beneath the ribs, reaching values up to 54.253 MPa for the parallel flow

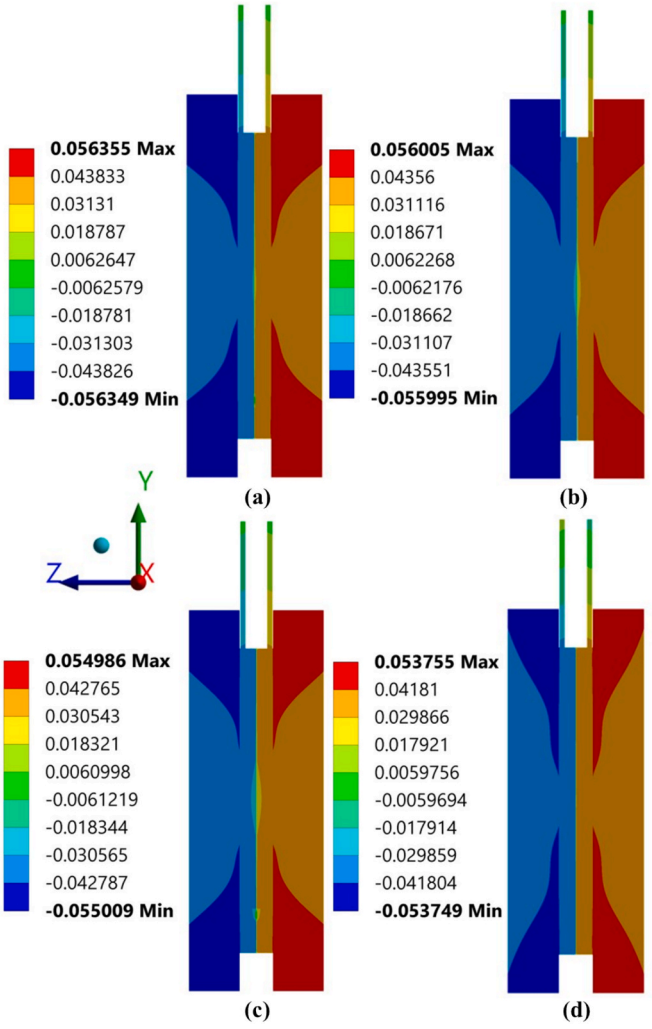

Fig. 14. Directional deformation distributions [mm] of the PEMFC under a clamping torque of 10 Nm and a temperature of 50 °C for different flow field configurations: (a) parallel, (b) spiral, (c) serpentine, and (d) pin-type.

field. The GDL experiences two primary compression zones: one located under the ribs, where mechanical deformation is dominant, and another under the flow channels, where the layer tends to expand slightly due to lower contact pressure. Excessive compression in the under-rib regions reduces the porosity and restricts gas diffusion, potentially leading to liquid–water accumulation and increased mass-transport resistance.

As shown in Fig. 8, the thermo-mechanical stress distribution on the cathode GDL strongly depends on the flow-field geometry. Among the analyzed configurations, the parallel design exhibits the highest maximum stress value of 54.428 MPa, primarily due to the non-uniform transfer of the clamping load along the straight channels and the limited lateral heat dissipation. In the spiral configuration, stress accumulation is observed near the central convergence region, reaching similarly high levels of 53.033 MPa. In contrast, the serpentine layout shows a more balanced stress distribution with a slightly lower peak value of 51.985 MPa, indicating improved mechanical compliance under combined thermal and torque loads.

The thermal stress analysis at 50 °C revealed that the cathode catalyst layer experiences maximum stress levels between 0.5 MPa and 1.0 MPa, consistent with the elastic range reported for PEMFC catalyst structures in previous studies [47]. Among the investigated geometries, the pin-type configuration exhibited the highest local stresses due to its discrete rib–channel pattern that induces non-uniform thermal expansion (see Fig. 9). In contrast, the parallel, spiral, and serpentine flow-field designs promoted a more uniform heat distribution, resulting in smoother thermal gradients and lower stress intensities across the catalyst layer. Overall, the predicted thermal stress field remains well below the mechanical strength threshold of the catalyst–membrane composite, confirming sufficient thermal stability under nominal operating temperature.

The effects of the applied clamping torque on the cathode catalyst layer (CCL) are presented in Fig. 10. The numerical analysis indicated that the pin-type flow-field configuration experienced the highest mechanical stress levels, while the serpentine design produced the lowest stress. Under a clamping torque of 10 Nm, the maximum von Mises stresses ranged from 14.9 MPa to 15.8 MPa, remaining below the tensile strength limit of the Pt/C–Nafion composite, approximately 25–30 MPa. A comparative analysis of the flow-field geometries revealed that transitioning from the pin-type to the serpentine configuration results in an approximately 5 % reduction in mechanical stress levels on the CL.

The combined effects of temperature and clamping torque on the CCL are depicted in Fig. 11. The results indicate that the coupled thermo-mechanical loading slightly alters the stress distribution pattern compared to the purely mechanical scenario, resulting in smoother gradients at the CL-membrane interface. The maximum thermo-mechanical stresses range from 14.4 to 15.0 MPa for all flow-field configurations, suggesting that the impact of thermal expansion at 50 °C is moderate relative to mechanical compression. The serpentine flow-field design shows the lowest stress level at approximately 14.447 MPa, signifying excellent structural compliance under mechanical compression and thermal loading.

The directional deformation distributions of the single-cell PEMFC under a clamping torque of 10 Nm indicate a clear dependence on the flow-field geometry, as shown in Fig. 12. When only the compressive torque loading is considered, the serpentine configuration exhibits the lowest overall deformation, whereas the pin-type flow-field shows the highest. Quantitatively, the grid-type model experiences approximately 4.58 % greater displacement than the serpentine design, highlighting the influence of rib–channel topology on the mechanical compliance of the cell stack. The deformation field reveals that the central region of the cell tends to bulge outward along the z-direction, resulting from the axial compressive forces applied at the bolt locations on the end plates. Maximum deformation occurs in the regions adjacent to the bolts, while the values gradually decrease toward the middle section of the cell along the y-axis, indicating a non-uniform load transfer across the assembly. This mechanical behavior suggests that optimizing the flow-field geometry and bolt layout is essential for achieving uniform compression, minimizing structural deflection, and ensuring long-term sealing integrity and electrochemical stability of the PEMFC.

Fig. 13 illustrates the directional deformation distributions of the PEMFC under only thermal loading at 50 °C, demonstrating that temperature-induced expansion significantly depends on the flow-field configuration. The highest levels of deformation are observed in pin-type, parallel, spiral, and serpentine flow-field designs, in that order. The grid-type configuration exhibits the most significant displacement due to localized thermal expansion near the rib–channel transition zones, while the serpentine geometry shows the lowest deformation, indicating superior structural compliance under thermal effects. A comparative analysis reveals that the deformation increases by approximately 71 % when transitioning from the serpentine to the grid-type configuration, emphasizing the influence of flow-field topology on thermal strain development. The deformation pattern reveals that positive displacements in the + Z direction are more pronounced in the cathode half-cell, whereas the anode side experiences the least deformation. This asymmetry arises from differences in the constituent materials' thermal expansion coefficients and the cell components' stacking sequence. The observed deformation gradient highlights the importance of thermal–mechanical compatibility between the bipolar plates, GDL, and membrane to maintain uniform stress distribution and prevent delamination or leakage at higher temperatures. Fig. 14 presents the

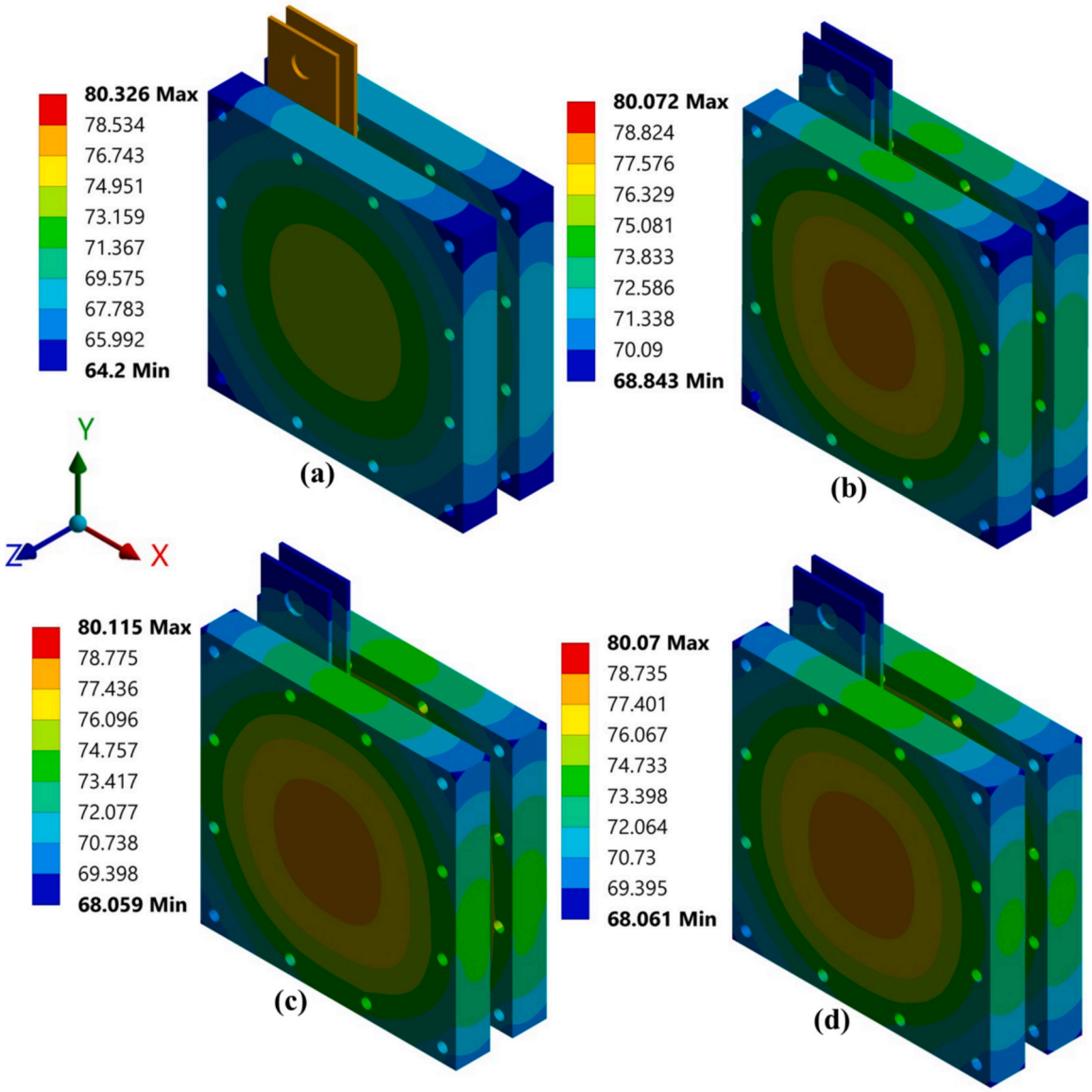

Fig. 15. Temperature distributions [°C] of the PEMFC at an operating temperature of 80 °C for different flow field configurations: (a) parallel, (b) spiral, (c) serpentine, and (d) pin-type.

numerical results of the combined effects of temperature and clamping torque on the directional deformations of the FEM models with different flow-field configurations. The analysis reveals that the thermally induced expansion of the cell components is partially compensated by the compressive deformation generated by the applied torque, resulting in a substantial reduction in the overall displacement compared to the case with mechanical loading alone. This interaction demonstrates a counteracting behavior between thermal and mechanical deformations, leading to improved structural stability of the assembly under coupled loading. Among the configurations examined, the parallel flow-field design experiences the highest total deformation, reaching up to 0.0563 mm, while both the serpentine and spiral designs exhibit more uniform and lower displacement distributions.

The thermal analysis of the numerical model was conducted using the ANSYS Steady-State Thermal module to assess the temperature distribution. The reactant flow regions were set to a temperature of 80 °C, and the resulting temperature fields for various flow-field configurations are shown in Fig. 15. Lower temperatures were observed near the bolt regions, where heat is effectively dissipated through metallic contacts. In contrast, the central zones exhibited higher temperature accumulation due to reduced convective heat removal. Among the designs examined, the parallel flow field provided the most uniform temperature distribution, characterized by minimal gradients and smooth color transitions across the active area. In comparison, the serpentine, spiral, and pin-type configurations displayed more pronounced temperature non-uniformities, primarily due to flow maldistribution, longer channel paths, and localized stagnation zones.

4. Conclusions

In this study, a three-dimensional finite element model was developed to investigate the thermal and mechanical behavior of PEMFCs with different flow field configurations under a constant clamping torque and various temperature loadings. The main results of the thermo-mechanical analysis can be outlined as follows:

1. The highest thermal stresses were observed in the pin-type flow field, reaching up to 1.98 MPa at 50 °C—approximately 65 % higher than those in the spiral configuration. Although these stresses remain below the tensile strength limit of the Nafion membrane, the

localized stress concentrations suggest that the pin-type design may exhibit lower mechanical durability and a higher risk of fatigue-induced degradation during prolonged operation. In contrast, the maximum coupled thermo-mechanical stress of about 12.2 MPa confirms that the membrane operates safely within its elastic range under combined loading conditions.

2. Mechanical stresses are higher beneath the rib regions, as they are the primary load-bearing areas under the applied clamping torque, while the channel openings provide less structural support.
3. The serpentine design exhibited the lowest stress levels, approximately 5–6 % lower than the pin-type design, while providing a more uniform pressure distribution and enhanced mechanical stability across the membrane surface.
4. The maximum mechanical stress in the cathode GDL reached 54.25 MPa under the parallel configuration, while the serpentine and spiral designs kept stress levels significantly below the strength limit of the carbon paper. In the catalyst layer, the thermo-mechanical stresses ranged from 14.4 to 15.0 MPa, indicating that the selected torque does not cause plastic deformation or interfacial delamination.
5. Considering the coupled influence of thermal and mechanical factors, the results revealed that a constant clamping torque of 10 Nm provides an optimal balance between the competing effects of temperature loadings, leading to lower thermo-mechanical stresses than mechanical loading.
6. The directional deformation analysis demonstrated that the maximum mechanical deformation occurred in the pin-type flow field model, reaching 0.068 mm, while the deformation induced by thermal loading was 0.032 mm, indicating that the mechanical load generated higher displacement compared to the temperature-induced expansion in the overall cell structure.

This study presents a comprehensive comparison of different flow-field channel configurations, demonstrating how the geometric layout has a significant impact on the thermo-mechanical stress behavior of the components of the PEMFC. The findings serve as practical guidance for developing more durable and reliable designs in PEMFCs.

CRediT authorship contribution statement

Safiye Nur Ozdemir: Writing – review & editing, Writing – original draft, Software, Resources, Methodology, Investigation, Data curation, Conceptualization. **Emre Kurt:** Writing – original draft, Validation, Software, Investigation. **Oguzhan Pektezel:** Writing – review & editing, Writing – original draft, Validation, Investigation, Data curation, Conceptualization. **Seçil Ekşi:** Writing – review & editing, Validation, Supervision, Methodology, Investigation.

Declaration of competing interest

The authors declare that they have no known competing financial interests or personal relationships that could have appeared to influence the work reported in this paper.

Data availability

The authors do not have permission to share data.

References

[1] Kim C, Na Y. Enhancing power density of PEMFC with narrow distribution zone using parallel serpentine hybrid flow field. Renew Energy 2025;241:122315.
[2] González GC, Toharias B, Rosa F, Guerra J, Iranzo A. Temperature and current density distributions in a 100 cm2 PEM fuel cell: effects of flow field designs. J Power Sources 2025;652:237625.
[3] Zhou J, Huang F, Wang W, Yang J, Ruan G. Numerical study and design optimization of geometry parameters of tesla valve flow fields for proton exchange membrane fuel cell. Energies 2025;18:5095.
[4] Ngo PM, Karimata T, Saitou T, Ito K. Effect of current density on membrane degradation under the combined chemical and mechanical stress test in the PEMFCs. J Power Sources 2023;556:232446.
[5] Sethy SK, Bhosale AC. A unique clamping mechanism for a cylindrical PEMFC for an enhanced performance. J Power Sources 2024;600:234258.
[6] Soriano RM, Rojas N, Nieto E, de Guadalupe González-Huerta R, Sandoval-Pineda JM. Influence of the gasket materials on the clamping pressure distribution in a PEM water electrolyzer: bolt torques and operation mode in pre-conditioning. Int J Hydrogen Energy 2021;46:25944–53.
[7] Wang Y, Sun Z, Yang L. Optimizing temperature distribution in a PEMFC stack: a computational study on cooling plate and coolant dynamics. Int J Hydrogen Energy 2025;97:88–103.
[8] Pashaie R, Shokrieh M, Vahedi M, Mirzaei A, Akbari S. A comparative study of residual stress measurement of laminated composites using FBG sensor DIC technique, and strain gauge. Opt Quant Electron 2024;56:1790.
[9] Ouaidat G, Cherouat A, Kouta R, Chamoret D. Study of the effect of mechanical uncertainties parameters on performance of PEMFC by coupling a 3D numerical multiphysics model and design of experiment. Int J Hydrogen Energy 2022;47:23772–86.
[10] Huo W, Wu P, Xie B, Du Q, Liang J, Qin Z, et al. Elucidating non-uniform assembling effect in large-scale PEM fuel cell by coupling mechanics and performance models. Energ Conver Manage 2023;277:116668.
[11] Khatir FA, Barzegari M, Talebi-Ghadikolaee H, Seddighi S. Integration of design of experiment and finite element method for the study of geometrical parameters in metallic bipolar plates for PEMFCs. Int J Hydrogen Energy 2021;46:39469–82.
[12] Uzundurukan A, Bilgili M, Devrim Y. Examination of compression effects on PEMFC performance by numerical and experimental analyses. Int J Hydrogen Energy 2020;45:35085–96.
[13] Ozdemir SN, Kurt E. A finite element modeling of PEMFC stack assembly under a novel hydraulic clamping mechanism. Environ Prog Sustain Energy 2025:e14649.
[14] Ouerghemmi M, Carral C, Mele P. Understanding the influence of MEA interfaces properties on PEMFC mechanical behavior through numerical analysis. Int J Hydrogen Energy 2024;69:242–51.
[15] Ma T, Jing G, Hu C, Qin Y, Sun X. Research on the mechanisms of contact resistance and structural deformation impact on PEMFC performance. Case Stud Therm Eng 2025;106845.
[16] G. Varghese, V.B. KP, T.V. Joseph, P. Chippar, A numerical investigation on thermal gradients and stresses in high temperature PEM fuel cell during start-up, International Journal of Heat and Mass Transfer 175 (2021) 121365.
[17] Zhang N, Chen W, Deng Q, Chen B. Pore-scale analysis of clamping force effects on microstructure and transport properties of PEMFC gas diffusion layers. Energ Conver Manage 2025;343:120218.
[18] Sun X, Wen P, Zhang Q, Jing G, Ma T. Numerical investigation of structural deformation of gas diffusion layer and contact resistance under assembly force effect on proton exchange membrane fuel cell performance. J Power Sources 2025;630:236120.
[19] Liu J, Tan J, Yang W, Li Y, Wang C. Better electrochemical performance of PEMFC under a novel pneumatic clamping mechanism. Energy 2021;229:120796.
[20] Bates A, Mukherjee S, Hwang S, Lee SC, Kwon O, Choi GH, et al. Simulation and experimental analysis of the clamping pressure distribution in a PEM fuel cell stack. Int J Hydrogen Energy 2013;38:6481–93.
[21] Zhang Z, Zhang J, Shi L, Zhang T. A study of contact pressure with thermo-mechanical coupled action for a full-dimensional PEMFC stack. Sustainability 2022;14:8593.
[22] Chippar P, Oh K, Kim D, Hong T-W, Kim W, Ju H. Coupled mechanical stress and multi-dimensional CFD analysis for high temperature proton exchange membrane fuel cells [HT-PEMFCs]. Int J Hydrogen Energy 2013;38:7715–24.
[23] Wen C-Y, Lin Y-S, Lu C-H. Experimental study of clamping effects on the performances of a single proton exchange membrane fuel cell and a 10-cell stack. J Power Sources 2009;192:475–85.
[24] Movahedi M, Ramiar A, Ranjber AA. 3D numerical investigation of clamping pressure effect on the performance of proton exchange membrane fuel cell with interdigitated flow field. Energy 2018;142:617–32.
[25] Zhou X, Qiu D, Peng L, Lai X. Numerical and experimental characterization of gas permeation through membranes with consideration of mechanical degradation in proton exchange membrane fuel cells. J Power Sources 2023;556:232489.
[26] Jing G, Hu C, Qin Y, Sun X, Ma T. Complex mechanisms of PEMFC performance variations influenced by both structural deformation and contact resistance under the clamping force. Int J Hydrogen Energy 2024;58:137–48.
[27] Cha D, Ahn JH, Kim HS, Kim Y. Effects of clamping force on the water transport and performance of a PEM (proton electrolyte membrane) fuel cell with relative humidity and current density. Energy 2015;93:1338–44.
[28] Wang R, Guan D, Cai X, Chen T, Chen Z. Effect of interfacial contact properties on the structural dynamics of PEMFC based on fractal theory and virtual material. J Alloy Compd 2024;1008:176658.
[29] Guan D, Pan B, Chen Z, Li J, Shen H, Pang H. Quantitative modeling and bio-inspired optimization the clamping load on the bipolar plate in PEMFC. Energy 2023;263:125951.
[30] Pan B, Guan D, Wang R, Chen Z, Chen T. A woodpecker-inspired assembly methodology for a proton exchange membrane fuel cell with uniform contact pressure on the bipolar plate. Energy Fuel 2024;38:23754–67.
[31] Cai X, Guan D, Zhang C, Zhou J, Chen T, Chen Z. Vibration induced multiscale damage mechanism of BPP: from interfacial electron transfer distortion to surface thermal ablation. Tribol Int 2025;110816.

[32] Guan D, Cai X, Zhang C, Pan B, Wang R, Li M, et al. Transient failure mechanism of bipolar plate using multiscale modeling considering the electrical contact of surface oxide film. Eng Fail Anal 2025;109884.
[33] Al-Baghdadi MAS. Three-dimensional solid mechanics-CFD modeling of a PEM fuel cell stack. Int J Energy Environ 2018;9:1–26.
[34] Habibnia M, Shakeri M, Nourouzi S. Determination of the effective parameters on the fuel cell efficiency, based on sealing behavior of the system. Int J Hydrogen Energy 2016;41:18147–56.
[35] Shang K, Han C, Jiang T, Chen Z. Numerical study of PEMFC heat and mass transfer characteristics based on roughness interface thermal resistance model. Int J Hydrogen Energy 2023;48:7460–75.
[36] Pianko-Oprych P, Zinko T, Jaworski Z. A numerical investigation of the thermal stresses of a planar solid oxide fuel cell. Materials 2016;9:814.
[37] Kusoglu A, Karlsson AM, Santare MH, Cleghorn S, Johnson WB. Mechanical response of fuel cell membranes subjected to a hygro-thermal cycle. J Power Sources 2006;161:987–96.
[38] Zhang Z, Tan Y, Yang D, Chu T, Li B. A finite element analysis model-based study on the effect of the frame on membrane stresses in proton exchange membrane fuel cells. Energies 2023;16:7044.
[39] Liepold H, Bird A, Heizmann PA, Fadlullah H, Nguyen H, Klose C, et al. High protonic resistance of hydrocarbon-based cathodes in PEM fuel cells under low humidity conditions: origin, implication, and mitigation. J Power Sources 2024;624:235537.
[40] Li Y, Liang L, Liu C, Li Y, Xing W, Sun J. Self-healing proton-exchange membranes composed of nafion–poly (vinyl alcohol) complexes for durable direct methanol fuel cells. Adv Mater 2018;30:1707146.
[41] Kundu S, Simon LC, Fowler M, Grot S. Mechanical properties of Nafion™ electrolyte membranes under hydrated conditions. Polymer 2005;46:11707–15.
[42] I.I. Inc., Properties of Pemion® Hydrocarbon Proton Exchange Membranes, Document ID: FM-6027-C, Revision C, Vancouver, Canada (2021).
[43] J.E.M. (Ed.), Polymer Data Handbook, second ed., Oxford University Press, New York (2009).
[44] Dafalla AM, Jiang F. Stresses and their impacts on proton exchange membrane fuel cells: a review. Int J Hydrogen Energy 2018;43:2327–48.
[45] Omongos RL, Galvez-Aranda DE, Zanotto FM, Vernes A, Franco AA. Machine learning-driven optimization of gas diffusion layer microstructure for PEM fuel cells. J Power Sources 2025;625:235583.
[46] Chen Y, Ke Y, Xia Y, Cho C. Investigation on mechanical properties of a carbon paper gas diffusion layer through a 3-D nonlinear and orthotropic constitutive model. Energies 2021;14:6341.
[47] Zhang J, Hu Y, Han C, Zhang H. Stress response and contact behavior of PEMFC during the assembly and working condition. Int J Hydrogen Energy 2021;46:30467–78.